PHYSICAL REVIEW B **95**, 195302 (2017)

Spin separation and exchange for quantum dots in the Overhauser field

J. Leśnicki[*] and B. Szafran[†]

AGH University of Science and Technology, Faculty of Physics and Applied Computer Science, al. Mickiewicza 30, 30-059 Kraków, Poland

(Received 20 January 2017; revised manuscript received 20 March 2017; published 2 May 2017)

We describe spin and charge dynamics of the system of two electrons confined within a double quantum dot defined in a quantum wire. The spin dynamics is driven by the electron motion in the presence of the spin-orbit interaction and the randomly varying local Overhauser field due to the nuclear spins. The Schroedinger equation is solved with the time-dependent configuration interaction method that allows for an exact description of the system dynamics. The procedures of the spin separation, exchange and read-out by the spin to charge conversion all induced by the detuning variation are simulated. The rates of the potential variation that are necessary for the spin separation and spin to charge conversion in the context of the Landau-Zener transitions are determined. The average over random configurations of the hyperfine field produces spin exchange results which qualitatively agree with the experimental data.

DOI: 10.1103/PhysRevB.95.195302

I. INTRODUCTION

Construction of a universal quantum gate for information processing on spins of electrons confined in quantum dots [1] requires implementation of a controllable coupling between the spins confined in adjacent quantum dots. The proposed procedure [2] employs time evolution of the system with switching on the exchange energy [3–7] J, defined as the difference of the singlet and triplet energy levels, for a short time. A nonzero exchange energy requires interdot tunnel coupling and can be achieved by modulation of the tunnel coupling between the dots with either a tunable interdot barrier [2] or tunable potential inside one or both quantum dots [8].

The exchange energy [2] in the absence of spin-orbit interaction and hyperfine interaction is isotropic [9], i.e., depends only on relative orientation of the spins and conserves the total spin in the dynamics of the few-electron systems. Variation of the spin polarization is possible in the presence of the spin-orbit coupling which translates the electron motion in space to rotations of its spin as it precesses in the effective magnetic field that accompanies the spin-orbit coupling [10–16]. The spin-orbit coupling allows also for initialization of the state of the spin qubits, for separation of the spins of moving electrons [17–19] in particular.

In the present paper we report on a simulation of the spin separation and spin exchange in a GaAs double quantum dot two-electron system. We use a quasi-one-dimensional model with the assumption of a strong lateral confinement and the time-dependent configuration-interaction approach that allows for an exact account of the two-electron spin and charge dynamics. For separation of the spins we use the texture of the internal magnetic field arising due to a nonzero magnetic moments of atomic nuclei [20–22]. The field is expressed as a local classical Overhauser field obtained by summation of randomly oriented nuclear magnetic moments over the span of the lateral electron wave function [23].

The coupling of the carrier spins to the changing nuclear spin field is considered the main source of dephasing and spin relaxation in III-V materials [20]. Here, the inhomogeneity of the nuclear field is used as a resource for separation of the spins, which is performed via an adiabatic evolution of the system kept in the ground state when the tunnel coupling between the dots is quenched. The exchange interaction is then switched on for the electrons to exchange their spins, as in Ref. [8]. Next, the procedure of the read out of the spin exchange result is implemented by projecting the spin states on the charge configurations of the double dot. The spin exchange probability averaged over a number of fluctuations of the Overhauser field reproduce the fringe pattern of the experimental results of Ref. [8] as a function of the potential difference in quantum dots (which is related to detuning ε) and the spin exchange time. We discuss the rate of the potential modulation for preparation of the initial states, the effects of the potential asymmetry on the exchange interaction, and the reproducibility of the spin manipulation procedures in the presence of the Rashba spin-orbit interaction and the Overhauser field.

The nuclear field fluctuates in time and reacts to the electron spins [20] which can induce the dynamical nuclear polarization processes [24–26] The dynamical polarization and the free fluctuations of the nuclear field occur at the time scales of $\simeq 100$ μs [24,27] which is much longer than procedures for the electron spin separation and exchange that we consider here that take a few μs at most, which justifies the assumption of the static field. Moreover, we consider here the case where the external magnetic field is oriented along the z axis of the wire along which the electron motion occurs, while the effective Rashba magnetic field is perpendicular to electron momentum. An absence of the dynamical nuclear polarization for the SO magnetic field perpendicular to the external one was demonstrated in Ref. [27]. The fluctuations of the field are taken into account by averaging over many runs with different random field distributions.

II. THEORY

We consider a quasi-one-dimensional double quantum dot defined within a GaAs quantum wire. The single-electron

---

[*] jan.lesnicki@fis.agh.edu.pl

[†] bszafran@agh.edu.pl

Hamiltonian for the considered system reads

$$\hat{H}_{3D(1)}(t) = \frac{\hbar^2\vec{k}^2}{2m^*} + V(\vec{r}) + \hat{H}_B + \hat{H}_{SO}, \tag{1}$$

with $\vec{k} = -i\nabla$, the electron effective mass in GaAs $m^* = 0.067\, m_0$, and $V(\vec{r})$ stands for the confinement potential. The third term ($\hat{H}_B$),

$$\hat{H}_B = \frac{g\mu_b}{2}\vec{\sigma}\cdot(\vec{B} + \vec{B}_{HF}(\vec{r})), \tag{2}$$

accounts for the spin Zeeman effect that includes the external magnetic field $\vec{B}$ and the internal Overhauser field due to the hyperfine interaction [20] with the nuclear spins, where $g = -0.44$ is the GaAs electron Landé factor, μ_b the Bohr magneton, and $\vec{\sigma}$ the vector of Pauli matrices. The last component of the Hamiltonian (1) is responsible for the Rashba-type spin-orbit coupling

$$\hat{H}_{SO} = \alpha(\sigma_z k_x - \sigma_x k_z). \tag{3}$$

We apply the coupling constant $\alpha = 0.44$ meV nm [23,28].

We assume that the system is strongly confined along the axis of the wire, so that the electrons occupy the ground state of the lateral quantization only and the charge dynamics involves time evolution exclusively in the axial direction. For the lateral single-electron wave functions we adapt the Gaussian form,

$$\Psi(x,y) = \frac{1}{\sqrt{\pi}l}\exp\left(-\frac{x^2+y^2}{2l^2}\right), \tag{4}$$

with $l = 10$ nm.

The Hamiltonian (1) neglects the orbital effects of the external field which is justified by the assumption of a strong lateral confinement. Based on this assumption we consider the electron wave functions frozen in the form given by Eq. (4) which allows us to introduce a quasi-one-dimensional version of the energy operator (1) obtained by integrating the Hamiltonian $\langle\Psi|\hat{H}_{3D(1)}|\Psi\rangle$ over x and y dimensions, which yields:

$$\begin{aligned}\hat{H}_{(1)} = {} & -\frac{\hbar^2}{2m^*}\frac{\partial^2}{\partial z^2} + V(z) + \frac{g\mu_b}{2}\vec{\sigma}\cdot(\vec{B} + \vec{B}_{HF}(z)) \\ & + i\alpha\sigma_x\frac{\partial}{\partial z},\end{aligned} \tag{5}$$

where $V(z)$ is the confinement potential along the axis of the wire [Fig. 1(a)], with two quantum dots of length L and R, separated by a barrier of length D. Two barrier regions fill the remainder of the computational box of length 213.6 nm. We took $L = R = 61.02$ nm and $D = 30.51$ nm for all the presented results. The potential is taken 0 inside the right quantum dot, 15 meV within the central barrier, and 100 meV in the outer barriers [Fig. 1(a)]. The potential in the left quantum dot is set equal to ΔV that is varied in the simulation.

In most of the calculations the external magnetic field is taken $|\vec{B}| = 100$ mT as in the experiments [7,8]. For this value not only the degeneracy between the triplet states is lifted, but also the nuclear spins separate from the electron spins in the sense that the electron-nuclear spin flips [20,22,29] are forbidden by the energy conservation. We approximate the hyperfine field by a local magnetic field of a random orientation which is considered constant during the time evolution of the electron spin. The latter assumption is justified by a long fluctuation time of the nuclear field which is of the order of 10 to 100 μs [20]. The fluctuation of the hyperfine field in the experimental conditions is accounted for by averaging the results of the spin dynamics, which is also used in the experimental data processing [8].

The procedure for derivation of the field $\vec{B}_{HF}(z)$ is adapted from Ref. [23] with a classical vector of the effective magnetic field of length 5 T generated at random orientation at each ion of the crystal followed by the averaging of all the local nuclear vectors with the probability density corresponding to the Gaussian lateral wave functions (4). A sample of the generated fields is plotted in Fig. 1(b). The values in Fig. 1(b) are given for each grid point in the finite difference approach that we employ for determination of the single-electron eigenstates. The effective HF field as seen by the electron spin is further reduced to a few milliteslas [21,22] by averaging over the probability density along the axis of the quantum dot.

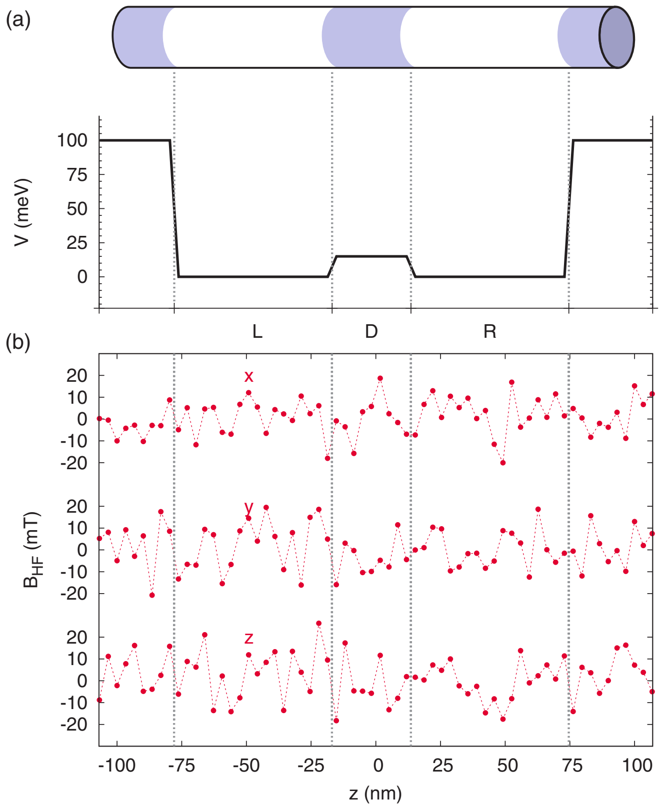

FIG. 1. (a) Schematic picture of a fragment of a quantum wire hosting a double quantum dot and its representation as a value of potential $V[z]$ along the z axis. (b) A sample of the effective HF magnetic (Overhauser) field generated at random with the approach of Ref. [23]. Each vector component (x, y, z) was plotted separately.

The integration of the two-electron stationary Hamiltonian over the lateral degrees of freedom produces the operator

$$\hat{H}^{(0)}_{(2)} = \sum_{i=1}^{2}\hat{H}_{(1)}(\sigma_i, z_i) + \frac{\sqrt{\pi/2}e^2}{4\pi\varepsilon_0\varepsilon l}\mathrm{erfcx}\left(\frac{|z_1 - z_2|}{\sqrt{2}l}\right), \tag{6}$$

where the last term is the electron-electron interaction potential that results from the integration of the Coulomb interaction with the lateral wave function [30], $\varepsilon = 12.9$ is the dielectric constant, and erfcx is the scaled complementary error function.

The two-electron Hamiltonian (6) is diagonalized by the configuration interaction method with the basis of Slater determinants χ_m of antisymmetrized products of the single-electron eigenfunctions of operator (5),

$$\psi_n(\sigma_1,\sigma_2,z_1,z_2) = \sum_{m=1}^{M} v_{nm}\,\chi_m(\sigma_1,\sigma_2,z_1,z_2). \qquad (7)$$

We used at least 120 Slater determinants for the basis (7) to obtain the eigenstates ψ_n and the energies of the two-electron Hamiltonian.

For simulation of the system dynamics we separate the external potential variation from the time-independent Hamiltonian,

$$\hat{H}_{(2)}(t) = \hat{H}^{(0)}_{(2)} + \hat{W}_{(2)}(t). \qquad (8)$$

The simulated potential variation amounts in changing the ΔV (additional left quantum dot potential)

$$\hat{W}_{(2)}(t) = \Delta V(t)\cdot(l(z_1) + l(z_2)), \qquad (9)$$

where $l(z)$ is equal to 1 in the left quantum dot and 0 elsewhere.

We solve the time-dependent Schrödinger equation

$$i\hbar\frac{\partial}{\partial t}\psi(t) = \hat{H}^{(0)}_{(2)}\psi(t) + \hat{W}_{(2)}(t)\psi(t), \qquad (10)$$

in the basis of $\hat{H}^{(0)}_{(2)}$ eigenstates ψ_n (7):

$$\psi(t) = \sum_{n=1}^{N} a_n(t)\psi_n(\sigma_1,\sigma_2,z_1,z_2)\exp\left(-iE_n t/\hbar\right). \qquad (11)$$

This form of the wave function when plugged into the Schrödinger equation produces a set of differential equations for the a_k coefficients,

$$\dot{a}_k(t) = -\frac{i}{\hbar}\sum_{n=1}^{N} a_n(t)\langle\psi_k|\hat{W}_{(2)}(t)|\psi_n\rangle e^{i(E_k-E_n)t/\hbar}, \qquad (12)$$

that we solve using the Crank-Nicolson scheme, for which the subsequent steps of the wave function are given by solution of an algebraic linear system of equations,

$$\left[I - \tfrac{1}{2}W(t+\Delta t)\Delta t\right]\vec{a}(t+\Delta t) = \left[I + \tfrac{1}{2}W(t)\Delta t\right]\vec{a}(t), \qquad (13)$$

with I that stands for the identity matrix, and $W(t)$ that stands for a matrix with elements

$$W_{k,n}(t) = -\frac{i}{\hbar}\Delta V(t)\langle\psi_k|l(z_1) + l(z_2)|\psi_n\rangle e^{i(E_k-E_n)t/\hbar}. \qquad (14)$$

The above method of integration is numerically exact, even for large values of ΔV, provided that a sufficient number of eigenstates is used in the basis. In the low-energy regime that we consider here $N = 20$ eigenstates in the basis are more than enough. Furthermore, recurring instantaneous ΔV switches followed by free evolutions were simulated by simply projecting the state ψ onto the new basis of eigenstates and updating phases of its components according to (11). The calculations of projections are summarized in Appendix.

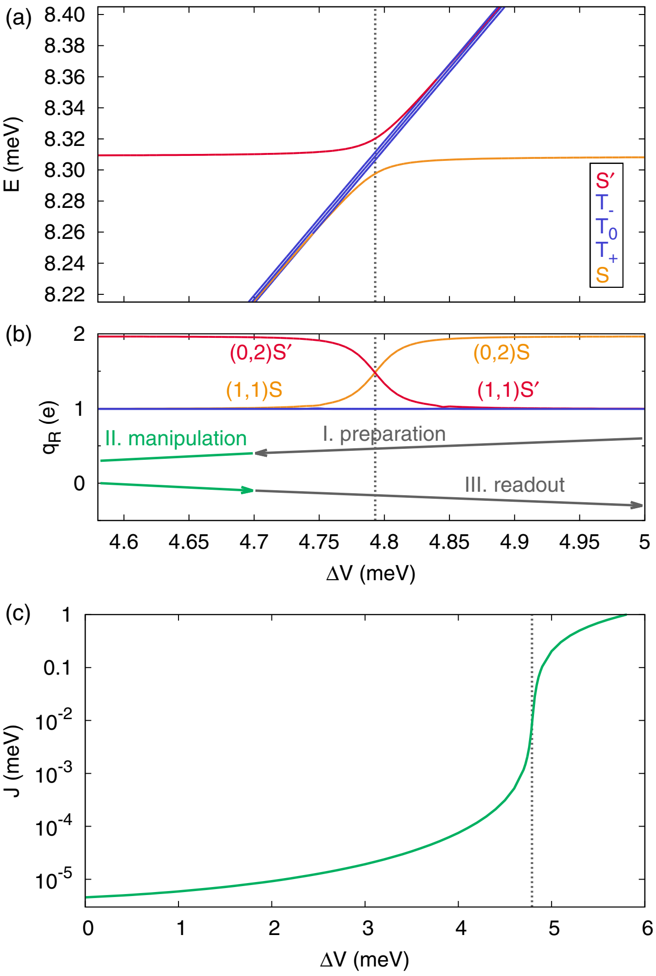

FIG. 2. (a) Energies E and (b) electron charge q_R stored by the right quantum dot, as functions of the potential difference ΔV. The sequence of ΔV changes is presented in (b). The system preparation amounts to an adiabatic charge transfer from (0,2)S state to the state with separated electrons (1,1)S. The manipulation of the state is carried at ΔV below the avoided crossing. For the readout of the spin state after the manipulation stage the system is ramped back to the voltages for which (0,2)S is the ground state. An axial magnetic field of $B_z = 100$ mT is applied here and below, unless stated otherwise. (c) The exchange energy J defined as the energy difference between T_0 and the lowest-energy singlet S. The center of the avoided crossing is marked by the vertical dotted line.

III. RESULTS

A. Two-electron eigenstates

The lowest two-electron energy levels are plotted in Fig. 2(a) as functions of the difference of potentials in left and right quantum dot. The charge localized in the right dot for the corresponding energy levels is plotted in Fig. 2(b). The splitting of the triplet energy levels in Fig. 2(a) is due to the axial magnetic field set to $B_z = 100$ mT. The spectrum in Fig. 2(a) contains the triplet states with a single electron per quantum dot [charge configuration denoted by (1,1)] as well

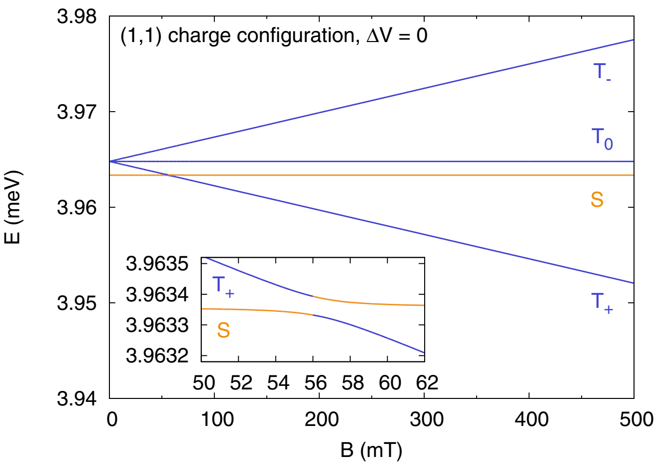

FIG. 3. Energies of the lowest four states of the system as a function of external magnetic field B. Inset shows enlarged anticrossing of states S and T_+. Curves are colored according to symmetry (singlet/triplet) and not to the actual order of states (which changes due to crossings).

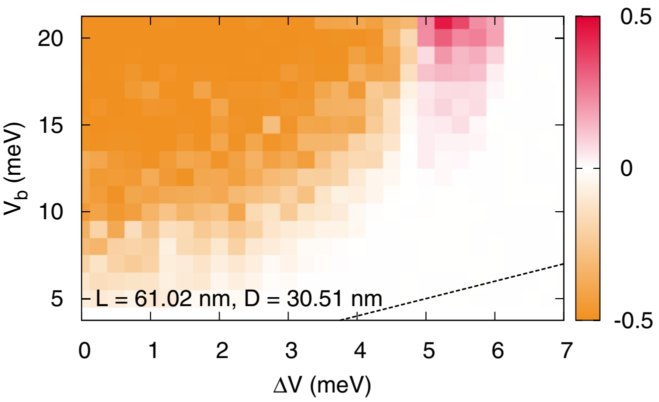

FIG. 4. Averaged absolute values of spin s_R in the right quantum dot in the second excited state, for different values of dot potential difference ΔV and barrier potential V_b. Values are taken with negative sign (orange) if the separation involves S and T_0 states, and with positive sign (red) when T_0 and S' are involved. The dashed line in the lower right corner marks the domain area for which the DQD is actually ill-defined since $V_b < \Delta V$.

as the singlet states with separated electrons (1,1)S, and both electrons localized in the right quantum dot (0,2)S (S' in the following denotes the higher-energy singlet state). Figure 2(a) shows an avoided crossing of the singlets near $\Delta V = 4.79$ meV. The (0,2)S energy level does not react to the potential variation in the left quantum dot with ΔV, hence its weak dependence on the potential variation outside the avoided crossing.

The magnetic field dependence of the energy levels with separated electrons—obtained for symmetric confining potential (i.e., for $\Delta V = 0$)—is depicted in Fig. 3. The narrow avoided crossing between the S and T_+ energy levels near 56 mT is induced by the spin mixing factors of the HF field and the SO coupling.

In the absence of the HF field and the SO coupling the wave functions of the two-electron eigenstates are separable into the spatial and spin components, in particular, for the states with zero total spin projection:

$$\Psi_S = \psi_S(z_1,z_2)\frac{1}{\sqrt{2}}(\chi_\uparrow(\sigma_1)\chi_\downarrow(\sigma_2) - \chi_\uparrow(\sigma_2)\chi_\downarrow(\sigma_1)), \quad (15)$$

and

$$\Psi_{T_0} = \psi_{T_0}(z_1,z_2)\frac{1}{\sqrt{2}}(\chi_\uparrow(\sigma_1)\chi_\downarrow(\sigma_2) + \chi_\uparrow(\sigma_2)\chi_\downarrow(\sigma_1)), \quad (16)$$

where χ are the spin eigenstates. For the states (15) and (16) the spin-up and spin-down densities are equal in each point in space, so that the dots store zero average spin. The spatial wave functions for states (15) and (16) can in the first approximation be expressed by the single-dot ϕ_l and ϕ_r ground-state orbitals, localized in the left and right dots, respectively,

$$\psi_S(z_1,z_2) = \frac{1}{\sqrt{2}}(\phi_l(z_1)\phi_r(z_2) + \phi_r(z_1)\phi_l(z_2)), \quad (17)$$

$$\psi_{T_0}(z_1,z_2) = \frac{1}{\sqrt{2}}(\phi_l(z_1)\phi_r(z_2) - \phi_r(z_1)\phi_l(z_2)). \quad (18)$$

In the weak interdot tunneling regime the S and T_0 states are nearly degenerate and can be mixed by either the spatial variation of the effective Landé g factor [31–33], the spin-orbit coupling [34], or the HF field [8]. For the maximal mixing case one obtains the spin separation over the dots

$$\begin{aligned}\Psi_{\uparrow\downarrow} &= \frac{1}{\sqrt{2}}(\Psi_S + \Psi_{T_0})\\ &= \frac{1}{\sqrt{2}}(\phi_l(z_1)\chi_\uparrow(\sigma_1)\phi_r(z_2)\chi_\downarrow(\sigma_2)\\ &\quad - \phi_l(z_2)\chi_\uparrow(\sigma_2)\phi_r(z_1)\chi_\downarrow(\sigma_1)) \quad (19)\end{aligned}$$

with the left (right) dot storing the spin-up (spin-down) density and a state with interchanged spins

$$\begin{aligned}\Psi_{\downarrow\uparrow} &= \frac{1}{\sqrt{2}}(\Psi_S - \Psi_{T_0})\\ &= \frac{1}{\sqrt{2}}(\phi_r(z_1)\chi_\uparrow(\sigma_1)\phi_l(z_2)\chi_\downarrow(\sigma_2)\\ &\quad - \phi_r(z_2)\chi_\uparrow(\sigma_2)\phi_l(z_1)\chi_\downarrow(\sigma_1)). \quad (20)\end{aligned}$$

The spin-orbit coupling alone can separate the spins over the dots in the external field but only provided that the double dot system is strongly asymmetric, with one dot larger by a factor of three than the other [34]. We find that the spin separation by the HF field occurs also for quantum dots of the same size. The average spin in the right dot calculated for the second excited state (T_0) is displayed in Fig. 4. The average was taken over five random HF field distributions. Naturally, for each random distribution the average spin in the left and right quantum dots is different. Note, that the experiment [8] also applies averaging the results of the spin evolution over many runs—for which the HF field varies. Figure 4 shows that for a high energy barrier the spin in the right dot is close to $|\langle S_z\rangle| = \frac{\hbar}{2}$, i.e., the spin separation is a typical result. We find that the spin configuration in the second excited state is then either ↑↓ or ↓↑, depending on the

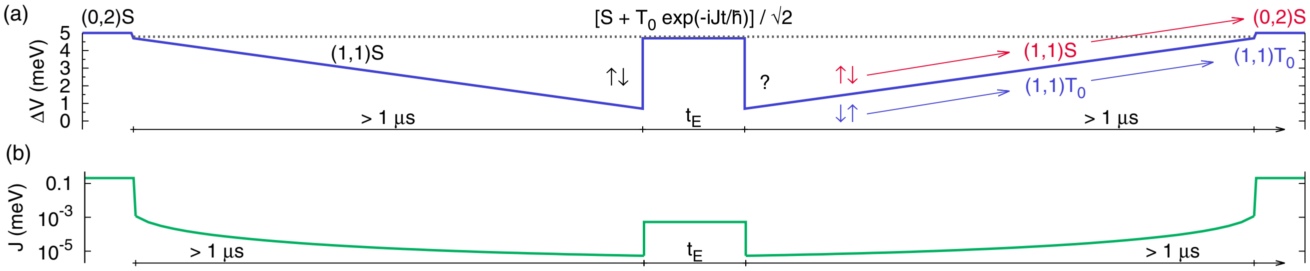

FIG. 5. (a) Variation of the potential asymmetry in time with the targeted evolution of the two-electron state explained schematically. (b) The exchange energy defined as the energy difference between the triplet T_0 state and the lowest energy singlet for the potential asymmetry in (a).

specific HF field distribution, the sign of the spin was hence neglected, instead, the values were taken as negative (orange) for the cases where the second state participating in the spin separation is the ground singlet S. In nanowire double quantum dots a substantial variation of the g factors in both the dots has been found [31–33]. The variation should fix the orientation of the spins in the Hamiltonian eigenstates in the absence of the exchange interaction. The spin separation in the Hamiltonian eigenstates is very rarely obtained for the ΔV values which correspond to the avoided crossing between the (1,1) and (0,2) singlets, near $\Delta V = 5$ meV. In this energy range the exchange energy is strong and prevails over the HF field fluctuations. Figure 4 shows that the closer we are to this value, the larger the interdot barrier V_b needs to be in order to induce the spin separation. The spin separation in the weak coupling regime is crucial for the charge and spin dynamics to be discussed below.

B. The spin separation and exchange sequence

The spin separation and exchange procedure that is simulated below is adapted from the experiment of Ref. [8] and depicted in Fig. 5. The procedure starts with a strong potential difference ΔV with two electron ground state singlets localized in the right quantum dot S(0,2). A slight change of ΔV is applied to pass across the singlets' avoided crossing of Fig. 2 with the evolution time that is fast on the time scale of the hyperfine field spin flipping but slow on the time scale defined by the exchange interaction, in order to change the charge occupation of the dots but keep the singlet spin state. Next, the symmetry of the confinement potential is restored slowly on the hyperfine interaction time scale, which—as we show below—in the presence of the HF field leads to the appearance of the state with definite spin orientation in each of the dots. Next, large asymmetry of the potential is reintroduced for the duration of t_E. The asymmetry of the confinement potential enhances the exchange interaction [35] and produces the spin flips between the dots as a result of time evolution of the superposition of (1,1)S and (1,1)T_0 states. After t_E the exchange energy is first rapidly quenched and then the potential is adiabatically changed towards the initial state.

The potential rise t_E in the experiment of Ref. [8] was surrounded by short intervals of a constant potential. For the present simulation of the slow adiabatic potential change conditions the intervals of a constant potential do not change the result, since at the end of the adiabatic evolution we have a well definite state of the instantaneous Hamiltonian which simply stays there when an interval of a constant potential is introduced. In a recent version of the experiment [7] the short intervals after the adiabatic change were skipped. The intervals of a constant potential do play a role when they are preceded by a nonadiabatic potential change—as in the exchange pulse, or in the spin echo procedure.

The right dot is occupied by two electrons with a maximal probability provided that an even number of spin flips was performed during the spin exchange time t_E. In the subsections to follow we first explain the electron structure of the eigenstates, next we move to the description of the system initialization, readout by the spin to charge conversion, and the interdot spin exchange.

C. Time evolution: Spin-dependent charge dynamics

The sequence that is simulated [see Fig. 2(b) and Fig. 5] starts as in the experiment [8] by the two-electron singlet with both electrons in the right dot (0,2)S. In this subsection we deal with the charge separation that is achieved by the small drop of ΔV from $\Delta V = 5$ meV to $\Delta V = 4.7$ meV that is visible at the beginning of the sequence in Fig. 5(a). The drop takes the system across the avoided crossing of the singlets in Fig. 2(a). The initial states are taken as eigenstates of the stationary Hamiltonian for $\Delta V = 5$ meV. The final state of the time evolution is plotted in Fig. 6(a)–6(d) as a function of the switching time for the first four eigenstates of the Hamiltonian for $\Delta V = 5$ meV and in terms of the eigenstates of the Hamiltonian for $\Delta V = 4.7$ meV (lower panels). Additionally, the resultant value of charge in the right dot (upper panels) is provided to emphasize states having (0,2) occupation. The rate of the changes can be compared with two time scales: the one given by the energy splitting between the singlets, which at the center of the avoided crossing [see Fig. 2(c)] is $\Delta S \simeq 0.02$ meV that corresponds to $\tau_E \simeq \frac{\hbar}{2\Delta S} = 16.5$ ps and the one given by the Zeeman splitting in the HF nuclear field of the singlet and T_+ state, $\Delta E_Z = g\mu_B B'_{HF}$, where B'_{HF} is given by averaging the nuclear magnetic field of Fig. 1(b) with the wave function along the z coordinate, typically $B'_{HF} = 1$ mT, for which $\tau_{HF} \simeq \frac{\hbar}{2\Delta E_z} = 12.9$ ns.

For the (0,2)S state as the initial state [Fig. 6(a)] the final one is (0,2)S$'$ when the switching is fast on the τ_S scale. The transition has then the Landau-Zener character [36–39]. The charge occupation of the dots is left unchanged for the nonadiabatic abrupt switching. To be more precise, the abrupt potential change leaves a small admixture of (1,1)S state to

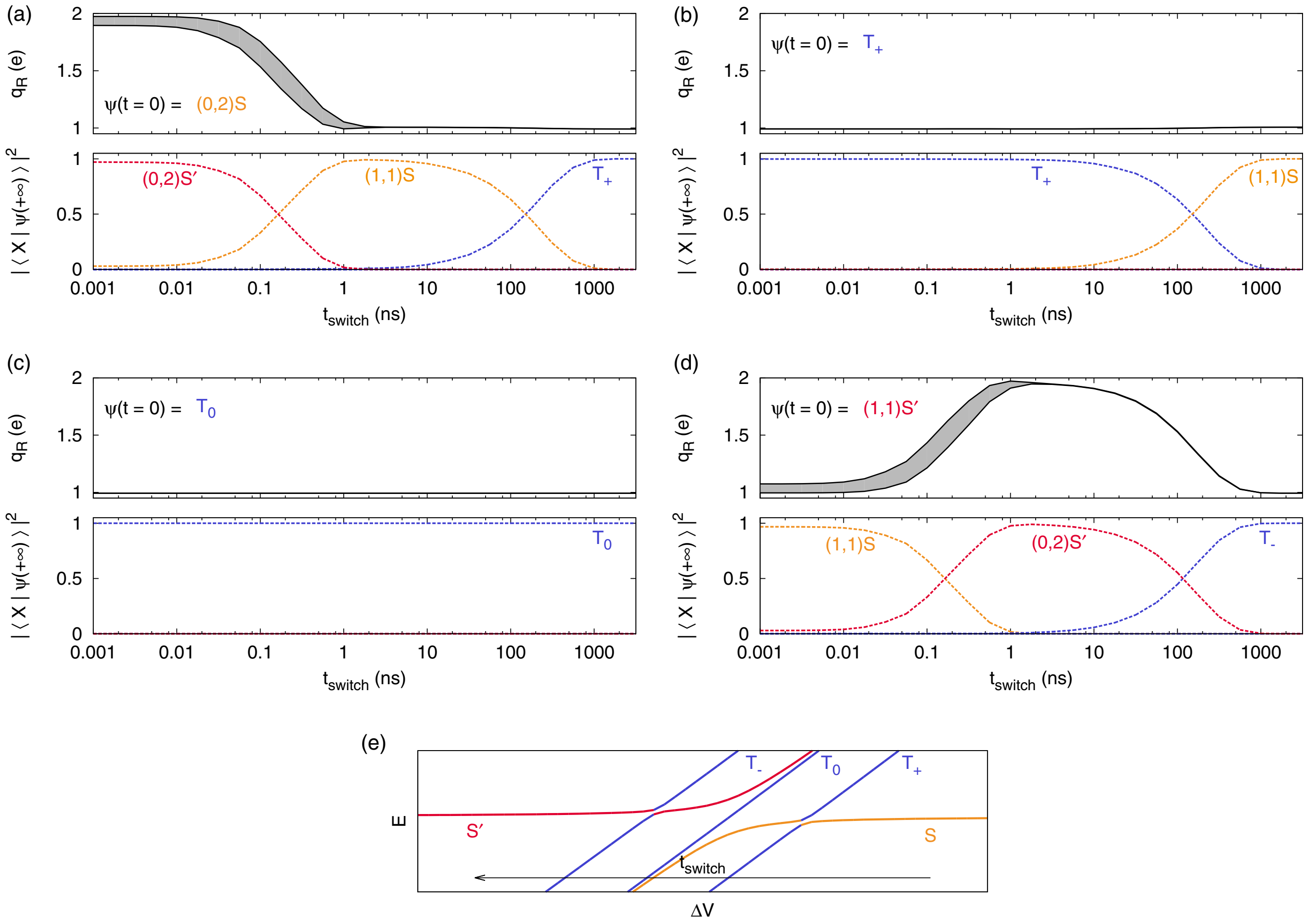

FIG. 6. Final absolute values of charge q_R in the right quantum dot (upper panels) and squared moduli of projections of final state $\psi(+\infty)$ onto the final Hamiltonian basis $X \in \{$S, T$_+$, T$_0$, T$_-$, S$'\}$ (lower panels), as a function of switching time t_{switch}, if the system was initially in the (a) (0,2)S, (b) T$_+$, (c) T$_0$, and (d) (1,1)S$'$ state. Potential difference ΔV was switched from 5.0 meV to 4.7 meV (state preparation). The gray areas in the upper panels of (a) and (d) indicate the range within which the charge in the right dot changes in the final state, which is a superposition of two final Hamiltonian eigenstates when the switching time is short. (e) The schematics of the spectrum and the switching direction.

(0,2)S$'$, which produces oscillations of the charge localized in the left dot in the limits that are marked in the upper panel of Fig. 6(a) with the gray area. For an adiabatic switching time comparable with τ_S the final state is the spin separated singlet (1,1)S, while for a very slow switching time—comparable with τ_{HF}—the evolution is adiabatic on the HF coupling time scale and the destination state is the T$_+$ ground state [see Fig. 6(e)]. Summarizing, Fig. 6(a) indicates a sequence of transitions across the two avoided crossings that involves both the (1,1) and (0,2) singlets as well as the T$_+$ triplet. The T$_+$$-S$ avoided crossing is much tighter than the (1,1)S and (0,2)S one, and thus it requires a much slower potential variation for the electron to pass from (0,2)S to the T$_+$ ground state. Conversely, for the initial state [Fig. 6(b)] set at T$_+$—an excited state at $\Delta V = 5$ meV—a very slow switching time $\simeq\tau_{HF}$ is required to keep the electron in the excited state [(0,2)S for lower ΔV], otherwise the time evolution ends at T$_+$ triplet. T$_0$ state does not enter any avoided crossing. For the initial state set at T$_0$ one stays in the T$_0$ independent of the switching time [Fig. 6(c)]. Finally, for (1,1)S$'$ in the initial state the final one is (1,1)S for a fast switching (much shorter than τ_S), (0,2)S$'$ for a longer switching time (between τ_S and τ_{HF}), and T$_-$ for an extremely slow ($\simeq\tau_{HF}$) switching. Therefore, both singlets in the initial state evolve to spin-polarized triplets in the limit of slow potential variation.

The time evolution presented in Fig. 6 with ΔV varied from 5 meV to 4.7 meV corresponds to the initial state preparation in the experimental sequence [8]. The reverse potential variation is used [8] in the spin state detection by the spin-charge conversion. In the experiment [8] the charge detection of the right quantum dot is used for determination of the result of the spin dynamics. The results of the simulation for the potential variation from $\Delta V = 4.7$ meV to $\Delta V = 5$ meV—the small and abrupt rise of the potential in the left dot at the end of the sequence of Fig. 5(a)—are given in Fig. 7. The initial state is set as one of the eigenstates of the Hamiltonian for $\Delta V = 4.7$ meV with the final states projected onto the Hamiltonian eigenstates for $\Delta V = 5$ meV. Figure 7 shows that the (1,1)S singlet evolves to (0,2)S only provided that the switching time is longer than $\simeq$0.1 ns but not longer than

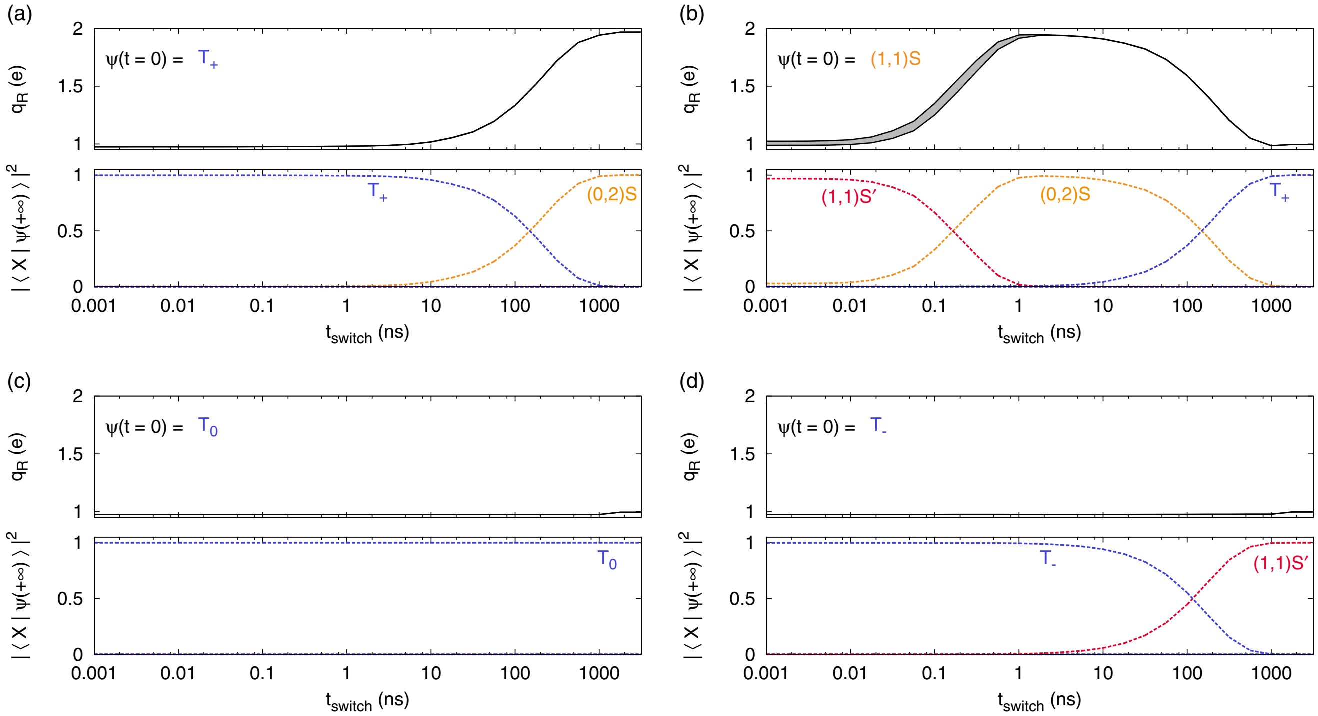

FIG. 7. Final absolute values of charge q_R in the right quantum dot (upper panels) and squared moduli of projections of final state $\psi(+\infty)$ onto the final Hamiltonian basis $X \in \{\mathrm{S}, \mathrm{T}_+, \mathrm{T}_0, \mathrm{T}_-, \mathrm{S}'\}$ (lower panels), as a function of switching time t_{switch}, if the system was initially in the (a) T_+, (b) (1,1)S, (c) T_0, and (d) T_- state. Potential difference ΔV was switched back from 4.7 meV to 5.0 meV (state readout).

$\simeq$200 ns. For a slower switching the system evolves to T_+. A slower switching time for T_+ in the initial state produces (0,2)S in the final state [Fig. 7(a)]. However, in order to produce a detectable increase of the charge in the right dot above a single electron charge, the switching time needs to exceed 10 ns. For T_- in the initial state a slow switching produces the spin singlet but with electrons separated over the dots [Fig. 7(d)].

The first two panels of Fig. 8 show the time evolution for the read-out sequence with the HF field switched off and the orientation of the external field changed to parallel to the x [Fig. 8(a)] and y directions [Fig. 8(b)]. For the x direction of the external field the spin of the two-electron state remains unchanged. In this case the effective SO magnetic field and the external field are aligned, so that the electron motion only changes the Zeeman splitting energy and no precession of the spin is present. For the external field oriented parallel to the y axis the precession reappears since the external and the effective fields are no longer aligned. In the presence of the HF interaction, the intrinsic anisotropy of the SO interaction is masked by the nuclear field, and the results remain quantitatively similar for varied external field orientation. However, the switching times differ within a certain range from one HF field configuration another. The results for three random configurations of the HF field are given in Figs. 8(c) and 8(d) with (d) or without (c) the SO interaction. The transition between the singlets—which are spin conserving—ignore the details of the HF field, however the transition to the spin polarized triplet does depend on the random HF field. Without the SO interaction the S-T_+ switching times differ by two orders of magnitude depending on the state of the nuclear field. The presence of the SO coupling reduces this variation range significantly to a single order of the magnitude only.

D. Time evolution: Spin separation

According to the preceding subsection the single-dot (0,2)S singlet can be transformed into the state with separated carriers (1,1)S provided that the switching time across the avoided crossing is of the order of 1 to 10 ns. For $\Delta V = 4.7$ meV considered above the spins are generally not polarized within the separate quantum dots (see Fig. 4). The spin separation in the system can then be induced by an adiabatic variation of the potential from $\Delta V = 4.7$ to 0.7 meV—see the part of the sequence with the slow potential difference drop in Fig. 5(a). The results for the system evolution are depicted in Fig. 9 for a typical random HF field. Figure 9 shows the projections of the final states in the basis of the destination Hamiltonian eigenstates. For the switching time that exceeds 100 ns the final states are the Hamiltonian eigenstates with separate spins, and there is one to one correspondence between the S and T_0 states to the ↑↓ and ↓↑ ones. Conversely, for the potential variation in the opposite direction one obtains either the S or T_0 state, depending on the spin distribution ↑↓ or ↓↑ in the left and right quantum dots, respectively. This fact is next used in the detection of the spin exchange with the spin and charge conversion induced by the potential variation. Obviously, the correspondence between S, T_0 and ↑↓, ↓↑ states can be opposite with equal probability for a random HF field distribution, however one or the other is typical for the

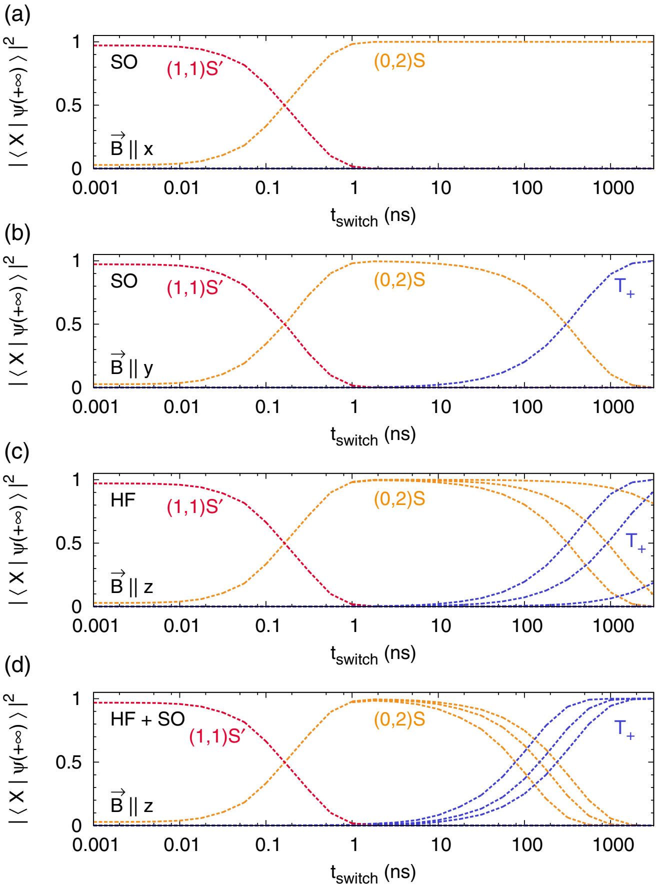

FIG. 8. Same as Fig. 7 for varied conditions of the simulation. The HF field is switched off (a),(b) and the magnetic field oriented parallel to the x (a) and y (b) directions. The SO interaction is switched off in (c). In (d) both interactions are present. Three random configurations of the HF field were considered in (c),(d).

HF field generated at random (i.e., spins tend to separate at low ΔV).

E. Time evolution: Spin exchange

Above we described how the system initialized in the (0,2)S ground state is taken across the avoided crossing to the (1,1)S state and next into the separated spin state ↑↓ or ↓↑, depending on the state of the HF field. Here, we consider the rapid rise of the difference of potentials (the center of Fig. 5) for which a nonzero exchange energy $J = E_{T_0} - E_S$ appears. Then, the solution of the time dependent Schrödinger equation reads

$$\Psi(t) = \frac{1}{\sqrt{2}} \exp\left(-\frac{i E_S t}{\hbar}\right)\left(\Psi_S + \Psi_{T_0} \exp\left(\frac{-iJt}{\hbar}\right)\right), \qquad (21)$$

and the spins in both the dots flip with the period of $T_f = \frac{2\pi\hbar}{J}$. The wave function of this form switches the spin orientations within the dot, as it varies from $\Psi_{\uparrow\downarrow}$ (at $t = 0$) to $\Psi_{\downarrow\uparrow}$ at $t = T/2$.

The spin flips are stopped when the system is taken down to a small value of ΔV again. For spin exchange times which are odd multiples of T_f, a slow rising of the potential takes the system to (1,1)T_0 eigenstates. For spin exchange times that are even multiples of T_f the potential variation returns the system to (1,1)S and next to (0,2)S.

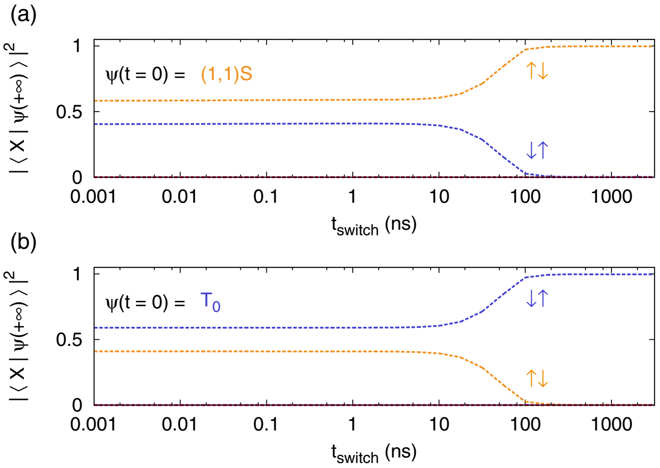

FIG. 9. Squared moduli of projections of final state $\psi(+\infty)$ onto the final Hamiltonian states with separated spins $X \in \{\uparrow\downarrow, \downarrow\uparrow\}$, as a function of switching time t_{switch}, if the system was initially in the (a) (1,1)S or (b) T_0 state. Potential difference ΔV was switched from 4.7 meV to 0.7 meV.

Figure 10 shows the projection of the wave function on $\Psi_{\uparrow\downarrow}$, taken as the initial state for the central high ΔV point in the time sequence as a function of time. The gray lines indicate three sample evolutions for some fixed random HF field orientations, and the green one is an average over 100 such runs. We can see that the average has a decreasing amplitude of the oscillations which corresponds to the inhomogeneous broadening due to the random field. In Fig. 11 we show the projection of the wave function on the $\Psi_{\uparrow\downarrow}$ state as a function of the potential difference ΔV during the spin exchange and the spin exchange time t_E. The inset shows the result obtained by Eq. (21) for the exchange energy as calculated in the absence of the HF field. The simulated pattern of the fringes agrees with the analytical one.

The result of the simulation contains the effect of the inhomogeneous potential—the visibility of the oscillations deteriorates with the exchange time. The oscillations are closer to the ideal value for a large potential variation ΔV in which the interdot tunnel coupling and the exchange energy is larger.

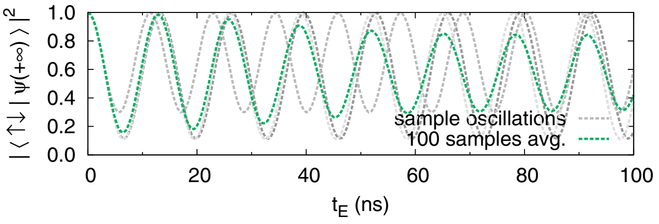

FIG. 10. Probabilities $P_S = |\langle S|\psi\rangle|^2$ of finding the system in state S as a function of exchange time t_E, for which larger potential difference was reintroduced (to $\Delta V = 4.5$ meV). Gray plots are sample Rabi oscillations, while the green is an average over 100 random distributions of the HF field.

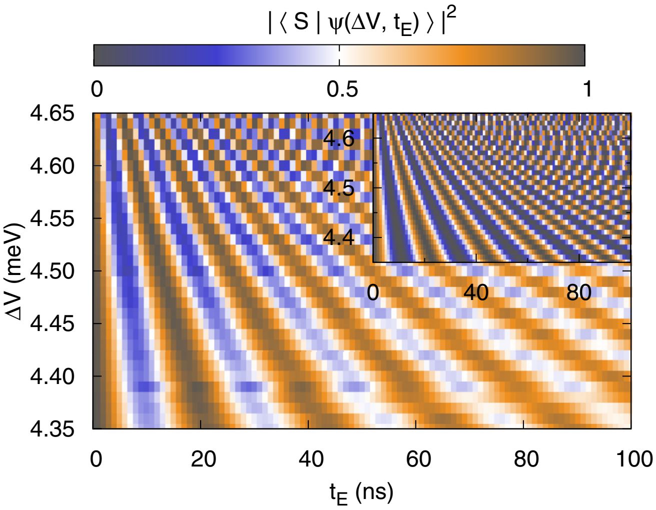

FIG. 11. Square of the absolute value of the projection of the wave function on the (1,1)S singlet state as a function of exchange time t_E and potential difference ΔV. Every horizontal strip of the plot is an average of 60 simulations, each run for different HF sample. Inset presents the results expected for the time evolution given by Eq. (21) for the exchange energy determined by the ΔV [see Fig. 2(c)].

The spin exchange is not only faster but occurs with the larger fidelity for larger ΔV, i.e., closer to the (1,1)-(0,2) avoided crossing.

F. Time evolution: Spin echo

Besides coherent spin exchange, the considered system is also suitable for performing spin-echo experiment [8]. Potential sequence for spin echo [Fig. 12(a)] comprises only rapid switches of ΔV. After the initialization in (0,2)S state, the system is brought to (1,1) charge distribution [below the dotted line in Fig 12(a)] and switched rapidly to a near-zero value of J, leading to a state being a superposition of $\uparrow\downarrow$ and $\downarrow\uparrow$ states [Fig. 9], which is then subject to dephasing due to the random nuclear field.

Dephasing may be reversed by applying a potential rise for a time sufficient to exchange the spins and then letting the system to evolve freely for the same amount of time (here 100 ns) it was previously allowed to dephase. By the end of the sequence the state is projected back onto (0,2)S and T_0 for readout.

Figure 12(b) presents the averaged results of 100 runs, for each potential value used for exchange (ranging from 4.35 to 4.65 meV), each run with different nuclear field sample used. Again, the plot presents the expected fringe pattern (as in the inset in the upper right corner) affected by inhomogeneity for both larger times t_E and lower exchange potential differences ΔV. The spin echo, unlike the spin exchange presented in Fig. 11, cannot transfer the system from singlet to T_0 state but only rephase it in the initial S state for t_E value being an odd multiple of T_f [30].

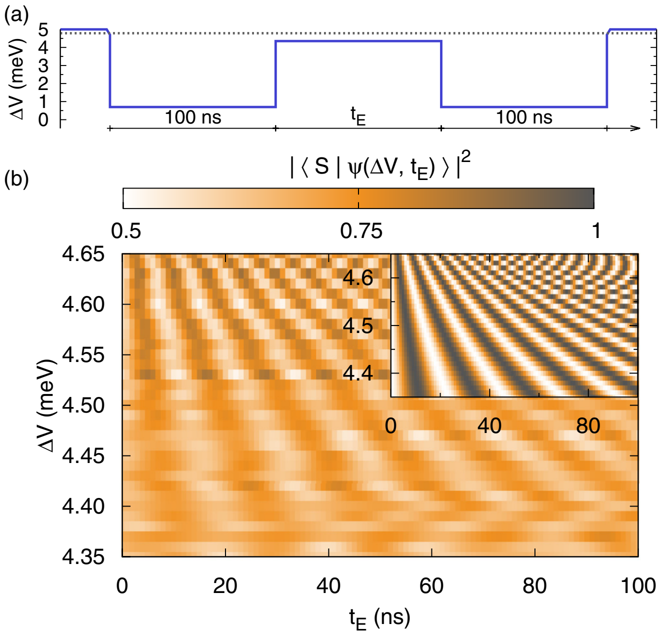

FIG. 12. (a) Sequence of potentials used to examine spin echo. (b) A plot, similar to Fig. 11, presenting probability of returning to state S after the operation versus ΔV and t_E of the central pulse (100 simulations were averaged to produce each horizontal strip). Inset presents the perfect behavior, according to Eq. (21).

IV. SUMMARY AND CONCLUSIONS

We presented simulation of the spin separation, exchange, and spin-to-charge conversion for a model of a two-electron system confined in a double quantum dot defined within GaAs quantum wire and a texture of the HF nuclear magnetic field with the SO interaction using the configuration interaction method and an effective Overhauser field distribution. For the potential difference (detuning) sweeps through the (0,2)S-(1,1)S avoided crossing—that is used for preparation of the initial state as well as for the spin to charge conversion applied for the readout, the HF field, and the SO interaction—play similar roles, and one can be replaced by the other. The transition times in HF field differ from one random distribution to the other, while the SO interaction introduces an anisotropy of the evolution in the external magnetic field. A simultaneous presence of the HF field and the SO interaction stabilize the variation range of the transition times and reduce the anisotropy as a function of the external magnetic field orientation.

The spin separation at the preparation stage is achieved due to the HF field and an adiabatic evolution at the scale of the nuclear Zeeman effect. The rate of the spin exchange induced by a pulse of potential ΔV differs strongly from one random nuclear spin distribution to another, but the averaged spin evolution closely follow the time scale set by the exchange energy in the absence of the HF field.

APPENDIX: STATE PROJECTION ONTO NEW BASIS

The applied method for the solution of the Schrödinger equation is based on an expansion of the wave function into a basis of the eigenstates of the Hamiltonian [Eq. (11)] for a fixed potential. The changes of the potential (rising and lowering) and their consequences are integrated in the chosen basis [Eq. (13)].

When the potential is rapidly changed and then kept constant—as for the exchange pulse—integration in the initial eigenstate basis would require a lot of computation while the solution in the target eigenstate basis is trivial. The basis is therefore changed on the course of the calculation.

Given a state $\psi(t)$ expressed as a superposition of eigenstates $\psi_0,\psi_1,\dots,\psi_N$ of the Hamiltonian for the initial potential [as in Eq. (11)] and wishing to re-express it in an eigenstate basis $\psi'_0,\psi'_1,\dots,\psi'_N$ of another Hamiltonian (with other potential difference ΔV), we write:

$$|\psi(t)\rangle = \sum_{n=1}^{N} a_n(t)|\psi_n\rangle e^{-iE_nt/\hbar} = \hat{I}\sum_{n=1}^{N} a_n(t)|\psi_n\rangle e^{-iE_nt/\hbar}$$

$$\approx \sum_{k=1}^{N} |\psi'_k\rangle\langle\psi'_k| \sum_{n=1}^{N} a_n(t)|\psi_n\rangle e^{-iE_nt/\hbar}. \tag{A1}$$

We may elaborate (A1) further, to obtain the state expressed in the new basis:

$$|\psi'(t)\rangle = \sum_{k=1}^{N} a'_k(t)|\psi'_k\rangle e^{-iE'_kt/\hbar}, \tag{A2}$$

where coefficients

$$a'_k(t) = \sum_{n=1}^{N} a_n(t)\langle\psi'_k|\psi_n\rangle e^{i(E'_k-E_n)t/\hbar}. \tag{A3}$$

One may find that integrals $\langle\psi'_k|\psi_n\rangle$ from the above equation are given by:

$$\langle\psi'_k|\psi_n\rangle = \sum_{l=1}^{M}\sum_{m=1}^{M} (v'_{kl})^* v_{nm}\langle\chi'_l|\chi_m\rangle, \tag{A4}$$

where χ'_l, χ_m are Slater determinants of single electron wave functions, and v'_{kl} and v_{nm} are coefficients of the expression of eigenstates ψ'_k and ψ_n in their respective Slater determinant bases of size M. Terms $\langle\chi'_l|\chi_m\rangle$ need to be numerically integrated for each pair of determinants χ'_l, χ_m, using their single-electron components.

[1] D. Loss and D. P. DiVincenzo, Phys. Rev. A **57**, 120 (1998).

[2] G. Burkard, D. Loss, and D. P. DiVincenzo, Phys. Rev. B **59**, 2070 (1999); G. Burkard, G. Seelig, and D. Loss, *ibid.* **62**, 2581 (2000).

[3] D. Bellucci, M. Rontani, F. Troiani, G. Goldoni, and E. Molinari, Phys. Rev. B **69**, 201308 (2004).

[4] X. Hu and S. Das Sarma, Phys. Rev. A **61**, 062301 (2000).

[5] A. Harju, S. Siljamaki, and R. M. Nieminen, Phys. Rev. Lett. **88**, 226804 (2002).

[6] B. M. Maune, M. G. Borselli, B. Huang, T. D. Ladd, P. W. Deelman, K. S. Holabird, A. A. Kiselev, I. Alvarado-Rodriguez, R. S. Ross, A. E. Schmitz, M. Sokolich, C. A. Watson, M. F. Gyureand, and A. T. Hunter, Nature (London) **481**, 344 (2012).

[7] B. Bertrand, H. Flentje, S. Takada, M. Yamamoto, S. Tarucha, A. Ludwig, A. D. Wieck, C. Bäuerle, and T. Meunier, Phys. Rev. Lett. **115**, 096801 (2015).

[8] J. R. Petta, A. C. Johnson, J. M. Taylor, E. A. Laird, A. Yacoby, M. D. Lukin, C. M. Marcus, M. P. Hanson, and A. C. Gossard, Science **309**, 2180 (2005).

[9] F. Baruffa, P. Stano, and J. Fabian, Phys. Rev. Lett. **104**, 126401 (2010).

[10] L. Meier, G. Salis, E. Gini, I. Shorubalko, and K. Ensslin, Phys. Rev. B **77**, 035305 (2008).

[11] C. Flindt, A. S. Sorensen, and K. Flensberg, Phys. Rev. Lett. **97**, 240501 (2006).

[12] P. Foldi, O. Kalman, M. G. Benedict, and F. M. Peeters, Nano Lett. **8**, 2556 (2008).

[13] A. Manchon, H. C. Koo, J. Nitta, S. M. Frolov, and R. A. Duine, Nat. Mater. **14**, 872 (2015).

[14] B. A. Bernevig, J. Orenstein, and S.-C. Zhang, Phys. Rev. Lett. **97**, 236601 (2006).

[15] J. D. Koralek, C. P. Weber, J. Orenstein, B. A. Bernevig, S.-C. Zhang, S. Mack, and D. D. Awschalom, Nature (London) **458**, 610 (2009).

[16] A. Sasaki, A. Sasaki, S. Nonaka, Y. Kunihashi, M. Kohda, T. Bauernfeind, T. Dollinger, K. Richter, and J. Nitta, Nat. Nanotech. **9**, 703 (2014).

[17] J. Pawlowski, P. Szumniak, A. Skubis, and S. Bednarek, J. Phys.: Condens. Matter **26**, 345302 (2014).

[18] S. Bednarek, P. Szumniak, and B. Szafran, Phys. Rev. B **82**, 235319 (2010).

[19] J. I. Ohe, M. Yamamoto, T. Ohtsuki, and J. Nitta, Phys. Rev. B **72**, 041308 (2005).

[20] R. Hanson, L. P. Kouwenhoven, J. R. Petta, S. Tarucha, and L. M. K. Vandersypen, Rev. Mod. Phys. **79**, 1217 (2007).

[21] A. S. Bracker, E. A. Stinaff, D. Gammon, M. E. Ware, J. G. Tischler, A. Shabaev, Al. L. Efros, D. Park, D. Gershoni, V. L. Korenev, and I. A. Merkulov, Phys. Rev. Lett. **94**, 047402 (2005).

[22] A. C. Johnson, J. R. Petta, J. M. Taylor, A. Yacoby, M. D. Lukin, C. M. Marcus, M. P. Hanson, and A. C. Gossard, Nature (London) **435**, 925 (2005).

[23] E. N. Osika, B. Szafran, and M. P. Nowak, Phys. Rev. B **88**, 165302 (2013).

[24] S. Foletti, H. Bluhm, D. Mahalu, V. Umansky, and A. Yacoby, Nat. Phys. **5**, 903 (2009); H. Bluhm, S. Foletti, D. Mahalu, V. Umansky, and A. Yacoby, Phys. Rev. Lett. **105**, 216803 (2010).

[25] I. Neder, M. S. Rudner, and B. I. Halperin, Phys. Rev. B **89**, 085403 (2014).

[26] M. J. Rancic and G. Burkard, Phys. Rev. B **90**, 245305 (2014).

[27] J. M. Nichol, S. P. Harvey, M. D. Shulman, A. Pal, V. Umansky, E. I. Rashba, B. I. Halperin, and A. Yacoby, Nat. Commun. **6**, 7682 (2015).

[28] E. A. de Andrada e Silva, G. C. La Rocca, and F. Bassani, Phys. Rev. B **55**, 16293 (1997).

[29] F. H. L. Koppens, J. A. Folk, J. M. Elzerman, R. Hanson, L. H. W. van Beveren, I. T. Vink, H. P. Tranitz, W. Wegscheider, L. P. Kouwenhoven, and L. M. K. Vandersypen, Science **309**, 1346 (2005).

[30] S. Bednarek, B. Szafran, T. Chwiej, and J. Adamowski, Phys. Rev. B **68**, 045328 (2003).

[31] M. D. Schroer, K. D. Petersson, M. Jung, and J. R. Petta, Phys. Rev. Lett. **107**, 176811 (2011).

[32] S. M. Frolov, J. Danon, S. Nadj-Perge, K. Zuo, J. W. W. van Tilburg, V. S. Pribiag, J. W. G. van den Berg, E. P. A. M. Bakkers, and L. P. Kouwenhoven, Phys. Rev. Lett. **109**, 236805 (2012).

[33] S. Nadj-Perge, V. S. Pribiag, J. W. G. van den Berg, K. Zuo, S. R. Plissard, E. P. A. M. Bakkers, S. M. Frolov, and L. P. Kouwenhoven, Phys. Rev. Lett. **108**, 166801 (2012).

[34] M. P. Nowak and B. Szafran, Phys. Rev. B **91**, 085102 (2015).

[35] B. Szafran, F. M. Peeters, and S. Bednarek, Phys. Rev. B **70**, 205318 (2004).

[36] H. Ribeiro and G. Burkard, Phys. Rev. Lett. **102**, 216802 (2009); H. Ribeiro, J. R. Petta, and G. Burkard, Phys. Rev. B **82**, 115445 (2010).

[37] J. R. Petta, H. Lu, and A. C. Gossard, Science **327**, 669 (2010).

[38] A. Mavalankar, T. Pei, E. M. Gauger, J. H. Warner, G. A. D. Briggs, and E. A. Laird, Phys. Rev. B **93**, 235428 (2016).

[39] S. N. Shevchenko, S. Ashhab and F. Nori, Phys. Rep. **492**, 1 (2010).